inorganics

MDPI

Article

Luminescent Water-Dispersible Nanoparticles Engineered from Copper(I) Halide Cluster Core and P,N-Ligand with an Optimal Balance between Stability and ROS Generation

Bulat A. Faizullin [1,*], Julia G. Elistratova [1], Igor D. Strelnik [1], Kamil D. Akhmadgaleev [1], Aidar T. Gubaidullin [1], Kirill V. Kholin [2,3], Irek R. Nizameev [3], Vasily M. Babaev [1], Syumbelya K. Amerhanova [1], Alexandra D. Voloshina [1], Tatiana P. Gerasimova [1], Andrey A. Karasik [1], Oleg G. Sinyashin [1] and Asiya R. Mustafina [1]

[1] Arbuzov Institute of Organic and Physical Chemistry, FRC Kazan Scientific Center of RAS, 8 Arbuzov Str., 420088 Kazan, Russia
[2] Department of Physics, Kazan National Research Technological University, 68 Karl Marx Str., 420015 Kazan, Russia
[3] Department of Nanotechnology in Electronics, Kazan National Research Technical University Named after A.N. Tupolev—KAI, 10 Karl Marx Str., 420111 Kazan, Russia
* Correspondence: bulat_fayzullin95@mail.ru

Abstract: The present work introduces the solvent exchange procedure as a route for conversion of the $Cu_4I_4L_2$ complex, where the Cu_4I_4 cluster core is coordinated with two P,N-ligands (L), into an aqueous colloid. The analysis of both colloidal and supernatant phases revealed some losses in CuI going from the initial $Cu_4I_4L_2$ complex to $Cu_2I_2L_3$-based nanoparticles. The comparative analysis of IR, ^{31}P NMR spectroscopy, ESI mass-spectrometry and luminescence data argued for a contribution of the "butterfly"-like structures of the Cu_2I_2 cluster core to $Cu_2I_2L_3$-based nanoparticles, although the amorphous nature of the latter restricted structure evaluation from the PXRD data. The green luminescence of the colloids revealed their chemical stability under pH variations in the solutions of some amino acids and peptides, and to specify the temperature and concentration conditions triggering the oxidative degradation of the nanoparticles. The spin trap-facilitated ESR study indicated that the oxidative transformations were followed by the generation of reactive oxygen species (ROS). The physiological temperature level (310 K) enhanced the ROS generation by nanoparticles, but the ROS level was suppressed in the solution of GSH at pH = 7.0. The cytotoxicity of nanoparticles was evaluated in the M-HeLa cell line and is discussed in correlation with their cell internalization and intracellular oxidative transformations.

Keywords: copper (I) halide cluster; P,N-ligand; hydrophilic nanoparticles; luminescence; ROS generation; chemodynamic therapy

check for updates

Citation: Faizullin, B.A.; Elistratova, J.G.; Strelnik, I.D.; Akhmadgaleev, K.D.; Gubaidullin, A.T.; Kholin, K.V.; Nizameev, I.R.; Babaev, V.M.; Amerhanova, S.K.; Voloshina, A.D.; et al. Luminescent Water-Dispersible Nanoparticles Engineered from Copper(I) Halide Cluster Core and P,N-Ligand with an Optimal Balance between Stability and ROS Generation. *Inorganics* **2023**, *11*, 141. https://doi.org/10.3390/inorganics11040141

Academic Editor: Rainer Winter

Received: 6 March 2023
Revised: 22 March 2023
Accepted: 23 March 2023
Published: 26 March 2023

Copyright: © 2023 by the authors. Licensee MDPI, Basel, Switzerland. This article is an open access article distributed under the terms and conditions of the Creative Commons Attribution (CC BY) license (https://creativecommons.org/licenses/by/4.0/).

1. Introduction

Complexes with halide-containing Cu_4I_4 cluster cores and bridging ligands bearing P and/or N–donor sites occupy a special place among Cu^I complexes due to their unique luminescent characteristics arising from ^{3}(M+X)LCT transitions from the cluster core, that result in a great diversity of stimuli-responsive luminescent properties [1–5], which are of significant impact on the development of sensors and cellular markers [6–9]. The antitumor potential of Cu^I complexes derives from the specific redox and coordinative transformations of Cu(I) ions [10–12]. Thus, the complexes with halide-containing Cu_nI_n cluster cores hold more potential in the design of antitumor agents than their mononuclear counterparts. In turn, the luminescence of such complexes prerequisites a visualization of their cell internalization. However, both low water solubility and easy redox and coordinative transformations of Cu^I complexes in aerated aqueous conditions restrict their use in aqueous

media. These restrictions can be overcome by developing specific ligand environment for the Cu^I ions in the relevant complexes, which is exemplified, but not limited, by diimine–phosphine or tris-hydroxymethylphosphine ligands [12,13]. Nevertheless, there are very few if any reports demonstrating the optimal ligand environment for Cu^I ions that combine the antitumor potential with luminescence, sufficient solubility in water and high chemical stability of Cu^I complexes.

Development of engineered nanomaterials is a strategy to enhance both chemical stability and biocompatibility of Cu^I complexes through their incorporation into nanoparticulate forms. The efficacy of nanomaterial engineering strategies is well demonstrated for inorganic Cu^I compounds, as exemplified by $Cu_{(2-x)}S$-based nanostructures [14,15], while the use of Cu^I complexes as the building blocks of engineered nanomaterials is growing day to day [11,12,16–18]. The encapsulation of the Cu^I complexes into liposomes demonstrates a fine example of the enhanced cell internalization of Cu^I complexes [18]. Moreover, the engineering of nanomaterials from d^{10}–complexes is already highlighted as the route for development of cellular markers and therapeutic agents [19–22].

It is worth noting that the oxidative transformations of Cu^I ions provide the basis of the so-called chemodynamic therapy (CDT), derived from the generation of reactive oxygen species (ROS) through Fenton-like reactions [11,14–20,23–25]. The CDT is a promising alternative to chemotherapy [15,23]. It is worth noting the reports highlighting the impact of P-donor and N,N-diimine systems as the ligand environment providing the chemical stabilization of Cu^I centers [11,16,17], although there are very few, if any, reports highlighting the engineered nanomaterial strategy as a tool to achieve the balance of the chemical stability of Cu^I complexes with their ROS-generation ability.

Thus, the present work demonstrates the previously reported luminescent Cu^I complex with 1,3-bis(benzhydryl)-5-(pyridine-2-yl)-1,3-diaza-5-phosphacyclohexane ligand ($Cu_4I_4L_2$) [2] (Figure 1) as the initial building block of hydrophilic nanoparticles suitable for cellular imaging and therapeutic applications. This complex is the convenient choice from the viewpoint of luminescent properties with high Stokes shift and microsecond lifetime of luminescence deriving from the triplet origin of the emission [2]. The ligand environment of two P,N-ligands in $Cu_4I_4L_2$ prerequisites the safety of this structural motif in solid form and in solution [26].

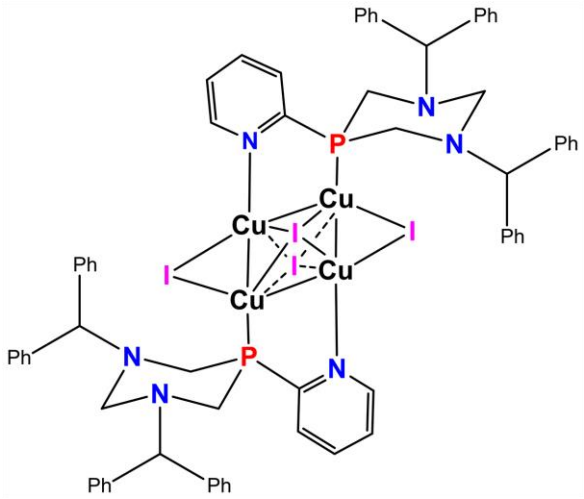


Figure 1. Schematically represented structural features of $Cu_4I_4L_2$ complex.

It is worth noting that the external factors affecting a CDT activity of Cu^I-based aqueous colloids, including those arising from their specific intracellular environment, are not recognized enough. Thus, the present work demonstrates the green luminescence of the produced colloids as an efficient tool to monitor their stability in acidified solutions, modeling the pH conditions in lysosomes, and glutathione and hydrogen peroxide solutions, modeling an intracellular environment. The ability of the nanoparticles to generate reactive

oxygen species (ROS) was monitored by the spin trap-facilitated ESR method in different conditions. The ROS generation of the Cu^I-based colloids in different conditions correlated with their oxidative degradations can reveal the main factors affecting the CDT activity of the colloids. The ability of the luminescent nanoparticles to visualize their cell internalization allows us to correlate the cytotoxicity of the nanoparticles with their chemical stability in the intracellular conditions.

2. Results and Discussion

2.1. Synthesis of F-127-$Cu_2I_2L_3$ Nanoparticles

Conversion of the molecular complexes into the nanoparticulate forms can be performed through the so-called solvent exchange procedure. The procedure is based on producing nanoprecipitates due to the self-assembly of water insoluble complexes under solvent exchange conditions, when an organic solution is mixed with an aqueous one. The procedure allows the researcher to control the size of nanoprecipitates by simple variation of the concentration conditions, including the organic-to-aqueous volume ratios. Thus, it has many applications in the conversion of water insoluble metal complexes into hydrophilic core–shell nanoparticles with high colloidal stability, where the hydrophilic shell derives from the adsorption of water soluble polymers [19,27,28]. The main advantage of such core–shell nanoparticles is the permeability of the non-covalently produced hydrophilic shell to small molecules, which facilitates their interaction with the luminescent complexes in the core which, in turn, generates both chemical and luminescent responses of the nanoparticles [19,27,28]. Taking into account the accessibility of Cu^I centers to oxygen and water molecules as the prerequisite of Fenton-like reactions [23–25], a covalent grafting of Cu^I complexes onto a silica surface is a possible alternate for the solvent exchange procedure, although the grafting is much more difficult to proceed than the aforesaid procedure. The precipitation of the Cu^I complex derives from the mixing of $Cu_4I_4L_2$ dissolved in DMF with the aqueous solution of NaI at a specific organic-to-aqueous volume ratio (for a more detailed synthetic procedure see the Materials and Methods section). The addition of NaI is aimed at restricting the release of the iodides in the synthetic conditions. The significant solubility of $Cu_4I_4L_2$ in DMF solutions is the main reason for the choice of DMF as the organic solvent.

The ^{31}P and ^{1}H NMR spectra of the Cu^I complex in DMF-d_7 and in acetone-d_6 solutions (Figures S1 and S2) indicate the chemical stability of the complex. However, the peaks in the spectrum measured in DMF-d_7 were significantly broadened in comparison with those in acetone-d_6, which indicates the greater extent of dissociative processes in DMF vs. acetone solutions. The addition of water into the DMF solution of $Cu_4I_4L_2$ triggered precipitation. The obtained precipitate was centrifuged and re-dissolved in DMF. The resulting ^{31}P NMR data indicate the presence of two peaks at ca. −38 and −30 ppm with the majority of the intensity in the latter (Figure S3). In the ^{1}H NMR spectra, the double set of peaks was registered in the region of the signals of pyridyl protons (9.5–8.0 ppm) indicative of the presence of the ligands with different coordinations towards the Cu^I ions, whereas other signals from the ligands were not informative.

The precipitated Cu^I complex formed a colloidal phase, which can be separated from the aqueous-organic solution through centrifugation. The phase separation allows us to wash out the nanoparticulate phase from water-soluble impurities. The ESI mass-spectrometry data obtained for both the initial and precipitated complex solutions also revealed the differences (Figures S4 and S5). In particular, the ESI mass spectrometry of the DMF solution of $Cu_4I_4L_2$ indicated the fragmentation of the complex to the following cations: $[2L+3Cu+2I]^+$, $[2L+2Cu+I]^+$, $[2L+Cu]^+$, $[L+2Cu+I]^+$ and $[L+Cu]^+$. The analogous fragmentation in the ESI mass spectrometry was observed for the relevant Cu^I complexes with the octahedral copper-halide core [2,8]. In the mass spectrum of the separated colloidal phase this fragmentation was not observed, whereas the major peak in the spectra (m/z 1794) corresponds to the molecular ion of the [3L+2Cu+I] composition. It is worth noting

that [3L+2Cu+I] ions have been reported in the previous articles on the $Cu_2I_2L_3$ complexes with the so-called "butterfly"-like copper halide core and the relevant P,N-ligands [29–31].

The significant amount of Cu^I ions in the supernatant was revealed by the ICP-OES analysis with very poor, if any, amount of phosphorous (Table S1). The Cu:P ratio in the separated nanoparticles was at the level of 2:3, calculated from the ICP-OES data. The IR spectrum of the dried colloids as a whole was close to the one for the $Cu_4I_4L_2$ complex, although the bands associated with stretching CC and CN vibrations of the pyridine moiety at 1598 and 1576 cm^{-1} differentiated the spectrum of $Cu_2I_2L_3$ from that of $Cu_4I_4L_2$ (Figure 2). The stretching CC and CN vibrations of the pyridine moiety at 1598 cm^{-1} arising from the coordinated pyridine are evident in both $Cu_4I_4L_2$ (Figure 2, spectrum 2) and $Cu_2I_2L_3$ (Figure 2, spectrum 3) (Figure 2). The band at 1576 cm^{-1} in the spectrum of $Cu_2I_2L_3$ coincides with the one observed in the free ligand spectrum (Figure 2, spectrum 1), which attributes the band to non-coordinated pyridine. Anyone can hypothesize the specific structure of $Cu_2I_2L_3$, where one ligand coordinates two Cu(I) ions via P,N-bridge mode, whereas two other ligands displayed only P-monodentate mode towards one of the Cu(I) ions. This coordination mode has been already reported for the complexes with a "butterfly"-like Cu_2I_2 halide core and the P,N-ligands [29–34].

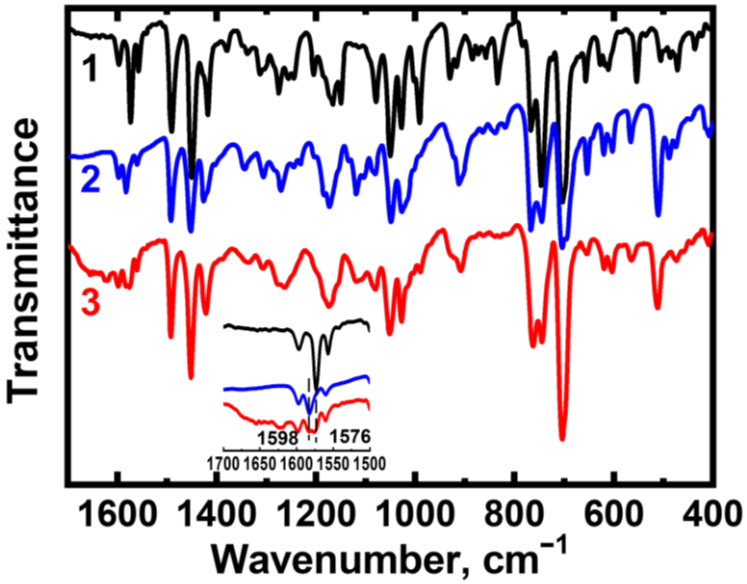


Figure 2. IR spectra of free ligand L (1), powder sample of $Cu_4I_4L_2$ (2) and dried $Cu_2I_2L_3$ colloids (3). Inset shows the region from 1700 to 1500 cm^{-1}.

The already documented diversity of phases revealed for the Cu^I complexes with a Cu_4I_4 cluster core derives from both distortions of the cluster core and formation of the crystalline solvates [2], which is evident from the different PXRD patterns simulated from the XRD data of the different crystalline phases (Figure S6). The PXRD pattern of the dried colloids represented by two amorphous 'galo' was quite different from the PXRD patterns of the crystalline samples of $Cu_4I_4L_2$ (Figure 3).

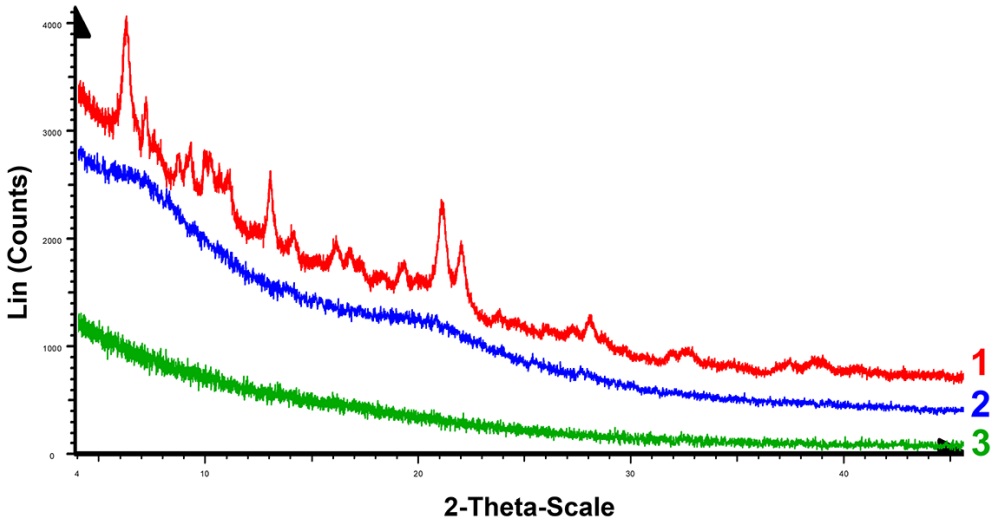
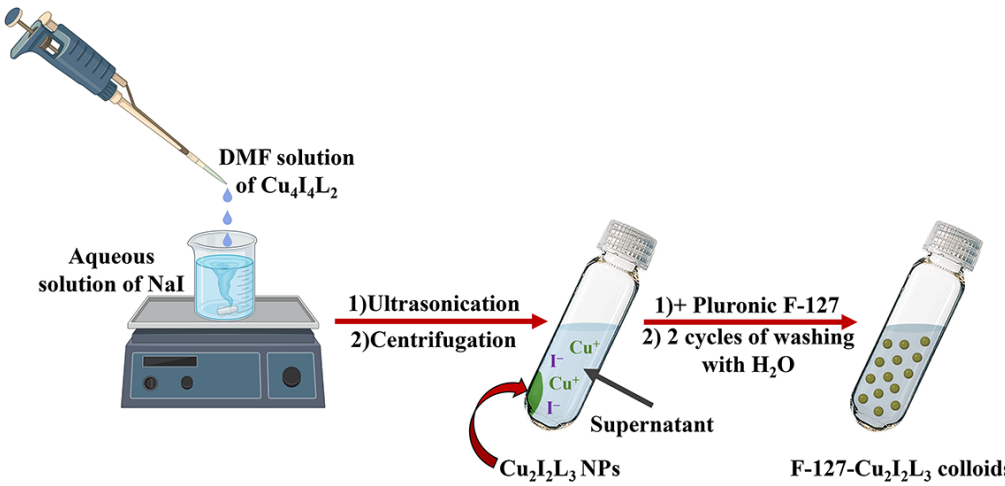


Figure 3. Experimental PXRD powder diffraction patterns of $Cu_4I_4L_2$ complex powder (1) and dried $Cu_2I_2L_3$ colloids (2). Curve 3 corresponds to the background scattering of a standard silicon wafer.

Moreover, the spectral and colloidal characteristics of the $Cu_2I_2L_3$-based nanoparticles were independent on the crystalline phase of the initial complex (Figure S7, Table S2). The aforesaid results indicate that the solvent exchange from the DMF to aqueous-DMF solution triggered the dissociation of the $Cu_4I_4L_2$ complex onto water-insoluble and water-soluble complex forms. It is worth assuming that the precipitation of $Cu_2I_2L_3$ is due to its lowest water solubility, while the copper content in the supernatant derives from the release of CuI in accordance with the mechanism shown in Scheme 1. Thus, the high thermodynamic stability of $Cu_4I_4L_2$ in DMF solutions cannot exclude its transformation into the $Cu_2I_2L_3$ form, although the widened peaks in the ^{1}H NMR spectra of the dried colloids dissolved in DMF-d_7 indicates that $Cu_2I_2L_3$ is less thermodynamically favorable than the initial complex in the same solvent.



Scheme 1. Schematic representation of F-127-$Cu_2I_2L_3$ nanoparticles preparation.

The as-prepared aqueous colloids exhibited green luminescence (Figure 4a) which was different from that of $Cu_4I_4L_2$ in DMF solution (Figure 4b) and the emission of $Cu_4I_4L_2$ in the solid state (492 nm) [2]. This difference derives from the chemical transformation of initial $Cu_4I_4L_2$ complexes into $Cu_2I_2L_3$-based nanoparticles in accordance with the cartoon illustration in Scheme 1. The lifetime of the excited state was evaluated from the time-resolved luminescence measurements in the aqueous solution of $Cu_2I_2L_3$-based colloids stabilized with F-127 (Figure S8). The obtained lifetime value (3.69 μs) fits to the

microsecond domain, which indicates the phosphorescent origin of the emission, and is similar to the lifetime values of the initial $Cu_4I_4L_2$ complex [2] and the complexes with a "butterfly"-like Cu_2I_2 halide core [5,29].

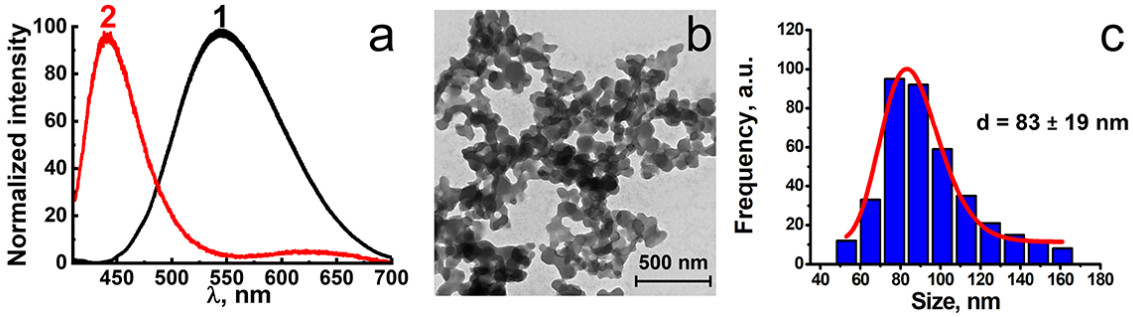


Figure 4. (**a**) Normalized intensity emission spectra of F-127-$Cu_2I_2L_3$ colloids (1) and DMF solution of $Cu_4I_4L_2$ complex (2). TEM image (**b**) and corresponding size distribution histogram (**c**) of dried F-127-$Cu_2I_2L_3$ colloids.

The amorphous nature of the dried colloids clearly argues for their difference from the initial complex, but excludes the analysis of the complex structure or structures corresponding to $Cu_2I_2L_3$ stoichiometry. However, the temperature-dependent luminescence exhibits its own specific features for different halide-containing Cu_4I_4 and Cu_2I_2 cluster cores. Thus, the temperature-resolved luminescence of the dried colloids was measured and compared with that of the initial complex. The main luminescence band at 560 nm excited at ca. 340 nm of the dried colloids tended to increase in intensity with decreasing temperature (Figure 5). This temperature-dependent behavior of the nanoparticles' emission is similar with that previously estimated for the complexes with a "butterfly"-like Cu_2I_2 halide core and P,N-ligands [5]. However, the temperature-induced spectral changes completely differed from those of the initial complex, for which showed the appearance of the additional bands in the emission spectra and redistribution of the population of two excited triplet levels following the decrease in temperature [2]. The aforesaid difference argues for the phase uniformity of $Cu_2I_2L_3$, where the freezing-induced rigidity of the structure is responsible for the temperature-dependent luminescence of the colloids.

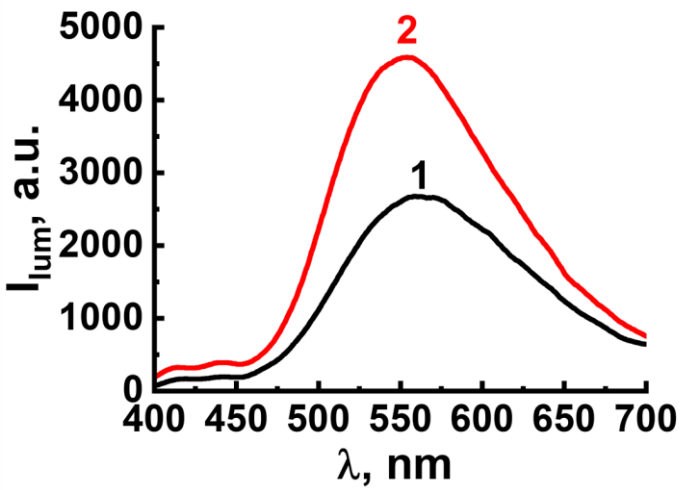


Figure 5. Solid-state emission spectra measured for the dried $Cu_2I_2L_3$-based colloids at room temperature (1) and at 77K (2).

The active surface of the as-obtained nanoparticles prerequisites their agglomeration, which can be minimized by a formation of a hydrophilic exterior layer. Indeed, the redispersion of the nanoparticles in the Pluronic F-127 solution resulted in the formation

of hydrophilic colloids, which hereafter will be designated as F-127-$Cu_2I_2L_3$. The DLS measurements of F-127-$Cu_2I_2L_3$ colloids revealed a low polydispersity index value with an average nanoparticle size of 186 ± 2 nm (Table 1). The TEM technique revealed the smaller average size (83 ± 19 nm) of the complex nanoprecipitates (Figure 4b,c) in comparison with the DLS data (Table 1). The aforesaid difference is explained by the thickness of the hydrophilic exterior layer resulting from the self-assembly of F-127 molecules onto the surface of the precipitated nanoparticles.

Table 1. Average diameter (d_{av}) and diameter values evaluated through the size distribution by number (d_{num}) measured by DLS, polydispersity indices (PDI) and electrokinetic potentials (ζ) of F-127-$Cu_2I_2L_3$ nanoparticles in pure water and buffered solutions.

	d_{av}, nm	d_{num}, nm	PDI	ζ, mV
H_2O	186 ± 2	163 ± 13	0.089 ± 0.024	+9 ± 8
Storage for 1.5 month:				
H_2O *	205 ± 2	165 ± 24	0.145 ± 0.006	−20 ± 6
H_2O **	170 ± 5	150 ± 7	0.075 ± 0.009	+11 ± 8
After heating colloids up to 40 °C:				
H_2O *	202 ± 3	158 ± 28	0.214 ± 0.006	−6 ± 4
H_2O **	186 ± 3	166 ± 1	0.129 ± 0.024	−20 ± 6
Buffered solutions:				
pH = 4	171 ± 4	151 ± 9	0.081 ± 0.012	+8 ± 7
pH = 4 ***	164 ± 5	151 ± 5	0.055 ± 0.022	+10 ± 6
pH = 7	170 ± 1	146 ± 8	0.086 ± 0.016	−5 ± 7
pH = 7 ***	172 ± 3	155 ± 2	0.098 ± 0.004	−4 ± 8
pH = 10	172 ± 4	144 ± 10	0.076 ± 0.012	−5 ± 7
pH = 10 ***	167 ± 3	149 ± 6	0.065 ± 0.012	−5 ± 8

* samples were prepared from diluted solutions. ** samples were prepared from concentrated solutions. *** after 2 days of storage.

The electrokinetic potentials of F-127-$Cu_2I_2L_3$ nanoparticles deviated from −6 mV to +11 mV, which indicates the electroneutrality of the colloid species (Table 1). However, the F-127-based hydrophilic layer of nanoparticles is the reason for both the low PDI values and insignificant increase in size in the buffered solutions.

2.2. Chemical Stability of F-127-$Cu_2I_2L_3$ Nanoparticles in Ambient Conditions and in Solutions Modeling Bioliquids

Both the stability of F-127-$Cu_2I_2L_3$ nanoparticles to oxidative transformation and the factors triggering the latter are of great impact on the capacity of the nanoparticles to generate ROS in the intracellular space or to undergo oxidative destruction before cell internalization. The storage of F-127-$Cu_2I_2L_3$ colloids (C = 20 μM) for one day resulted in the decreased intensity of the emission band and the luminescence of F-127-$Cu_2I_2L_3$ remained on a significant level after storage for 21 days (Figure 6a). However, the similar band of the concentrated colloids (C = 200 μM) remained unchanged after the same storage time in ambient conditions (Figure 6b). This indicates that the concentration-enhanced aggregation of F-127-$Cu_2I_2L_3$ nanoparticles provides the reason for the decreased accessibility of the surface-exposed Cu^I ions to interaction with oxygen and water molecules. Thus, the oxidative degradation of the nanoparticles is a time-consuming process, which can be retarded by the storage of colloids in the concentrated conditions. Moreover, the colloidal characteristics of F-127-$Cu_2I_2L_3$ nanoparticles remained practically unchanged after storage for 1.5 month in aqueous solutions and for two days in buffered solutions (Table 1), which is further confirmation of their chemical stability.

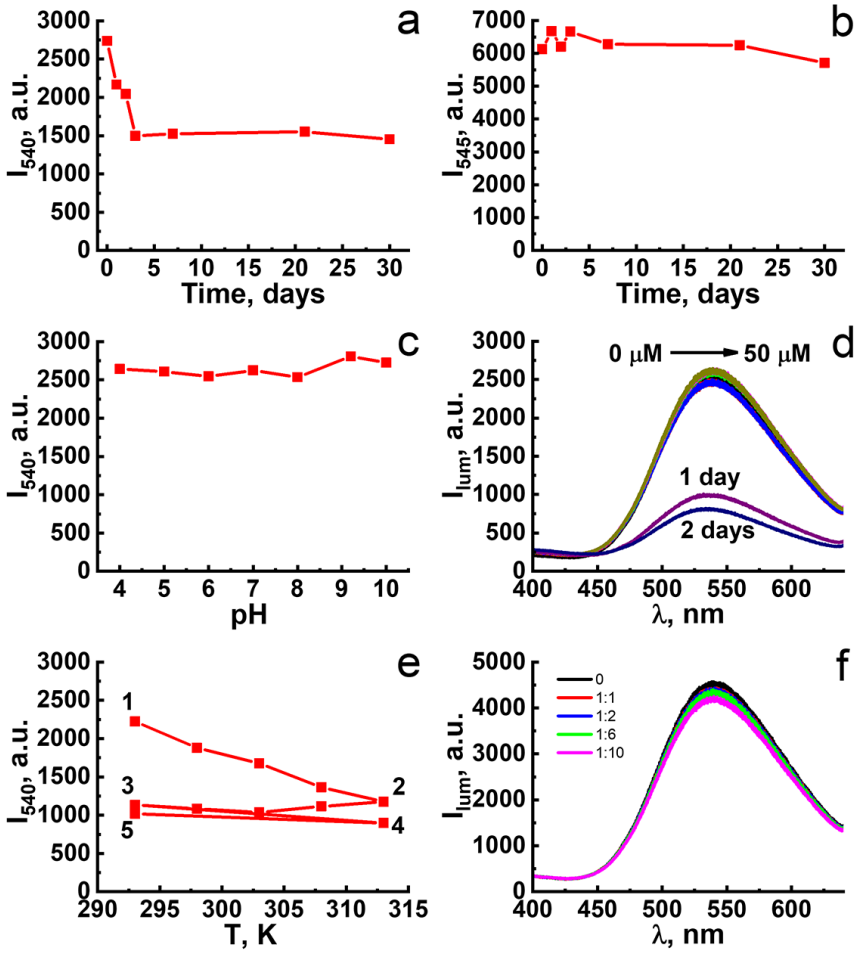


Figure 6. Emission intensities of diluted (**a**, C = 20 μM) and concentrated (**b**, C = 200 μM) F-127-$Cu_2I_2L_3$ colloids versus storage time. (**c**) Emission intensities of F-127-$Cu_2I_2L_3$ colloids (C = 20 μM) in solutions at different pH values. (**d**) Luminescence spectra of F-127-$Cu_2I_2L_3$ colloids (C = 20 μM) in the presence of H_2O_2. (**e**) Emission intensities of F-127-$Cu_2I_2L_3$ colloids (C = 20 μM) at different temperatures: 1-2-3—first heating–cooling cycle, 3-4-5—second heating–cooling cycle. (**f**) Luminescence spectra of F-127-$Cu_2I_2L_3$ colloids (C = 40 μM, pH = 7.0) at different concentrations of GSH designated as molar ratios Cu:GSH in Figure legend. λex are 330 nm and 365 nm for diluted and concentrated solutions, respectively.

It is worth noting that the stimuli-induced oxidative transformations of F-127-$Cu_2I_2L_3$ nanoparticles can result in Fenton-like reactions due to Equations (1) and (2):

$$2Cu^+ + O_2 + 2H^+ \rightleftarrows 2Cu^{2+} + H_2O_2 \quad (1)$$

$$Cu^+ + H_2O_2 + H^+ \rightleftarrows Cu^{2+} + OH\cdot + H_2O \quad (2)$$

The abovementioned sensitivity of F-127-$Cu_2I_2L_3$ luminescence to oxidative transformations allows us to use the luminescence response to external stimuli as a tool to reveal the efficacy of the Fenton-like reactions under different pH, concentration of H_2O_2 and temperature conditions. The luminescence of F-127-$Cu_2I_2L_3$ nanoparticles is invariant in the buffer solutions under the pHs ranging from 4.0 to 10.0 (Figure 6c) and in the as-prepared solutions of H_2O_2 even at 50 μM, while their storage for one day resulted in the pronounced degradation of the luminescence (Figure 6d). This indicates that the nanoparticulate state of $Cu_2I_2L_3$ complexes slows down their oxidative degradation in H_2O_2 solutions.

Quick and irreversible quenching was observed under the heating of F-127-$Cu_2I_2L_3$ colloids (C = 20 μM) up to 313 K (Figure 6e), which points to the possibility of ROS generation in physiological temperature conditions. This fact suggests that the gentle heating of F-127-$Cu_2I_2L_3$ within the physiological temperature range is the trigger for ROS generation. Nevertheless, the heating-induced degradation of the nanoparticles at the higher concentrations (C = 200 μM) was less pronounced (Figure S9) than the degradation of the diluted colloids. However, the concentration-enhanced aggregation of F-127-$Cu_2I_2L_3$ nanoparticles could slow down the temperature-induced oxidative degradation of the latter.

These results point to the oxidative degradation of F-127-$Cu_2I_2L_3$ being enhanced in heating conditions as the possible reason for ROS generation, which can trigger an apoptotic mechanism of cell death. However, the studies of cellular uptake and cytotoxicity of F-127-$Cu_2I_2L_3$ nanoparticles should be preceded by monitoring of their coordinative degradation in solutions of amino acids and proteins modeling a nutrient medium. Thus, the luminescence of F-127-$Cu_2I_2L_3$ was monitored in buffered solutions containing lysine, arginine, histidine, cysteine and tripeptide glutathione (GSH) under various concentrations and in a solution of bovine serum albumin (BSA) (Figure 6f and Figure S10). The results (Figure S10) indicate that the presence of lysine, arginine, histidine and BSA at various concentrations resulted in rather small quenching of the emission band of F-127-$Cu_2I_2L_3$. However, the high level of the intracellular antioxidants, mainly represented by GSH [35], can induce coordinative transformations of the nanoparticles in the cell cytoplasm. The high coordinative potential of both oxidized and reduced forms of glutathione [36–38] prerequisites the greater quenching of the nanoparticles' emission in solutions of GSH. However, the quenching effect was rather small even with ten-fold excess of GSH, but tended to increase within 30 min (Figure 7).

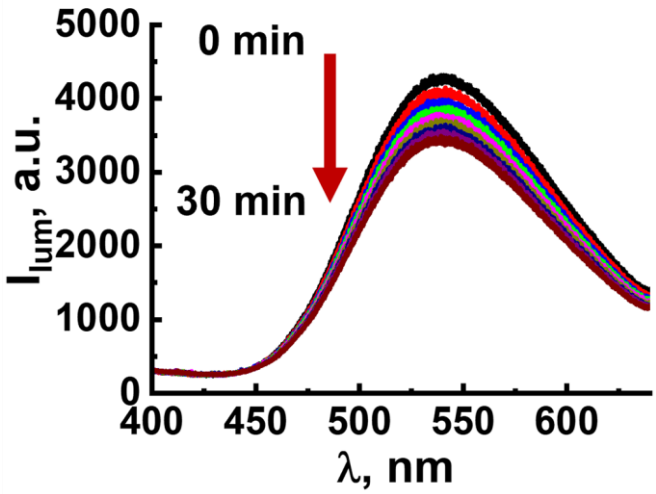


Figure 7. Luminescence spectra of F-127-$Cu_2I_2L_3$ colloids (C = 40 μM, pH = 7.0) in the presence of ten-fold excess of GSH, recorded within 30 min after the sample preparation.

2.3. ROS Generation by F-127-$Cu_2I_2L_3$ Nanoparticles

The ESR technique facilitated by the use of the spin traps is a powerful tool in detecting ROS [39,40], including those generated by Cu^I ions [41].

ROS generation by F-127-$Cu_2I_2L_3$ nanoparticles was monitored through the spin trap (5,5-Dimethyl-1-Pyrroline-N-Oxide (DMPO))-facilitated ESR technique under both ambient and specific temperature and concentration conditions to facilitate the oxidative degradation of F-127-$Cu_2I_2L_3$ in order to confirm the relationship between the oxidative degradation and ROS generation (Figure 8). The latter produced very short-lived hydroxyl radicals (OH·) in aqueous solutions, which can be monitored via the long living DMPO-OH· adduct (g = 2.0055, aN = 14.9 G, aH = 14.9 G, ΔH = 1.2 G) [42].

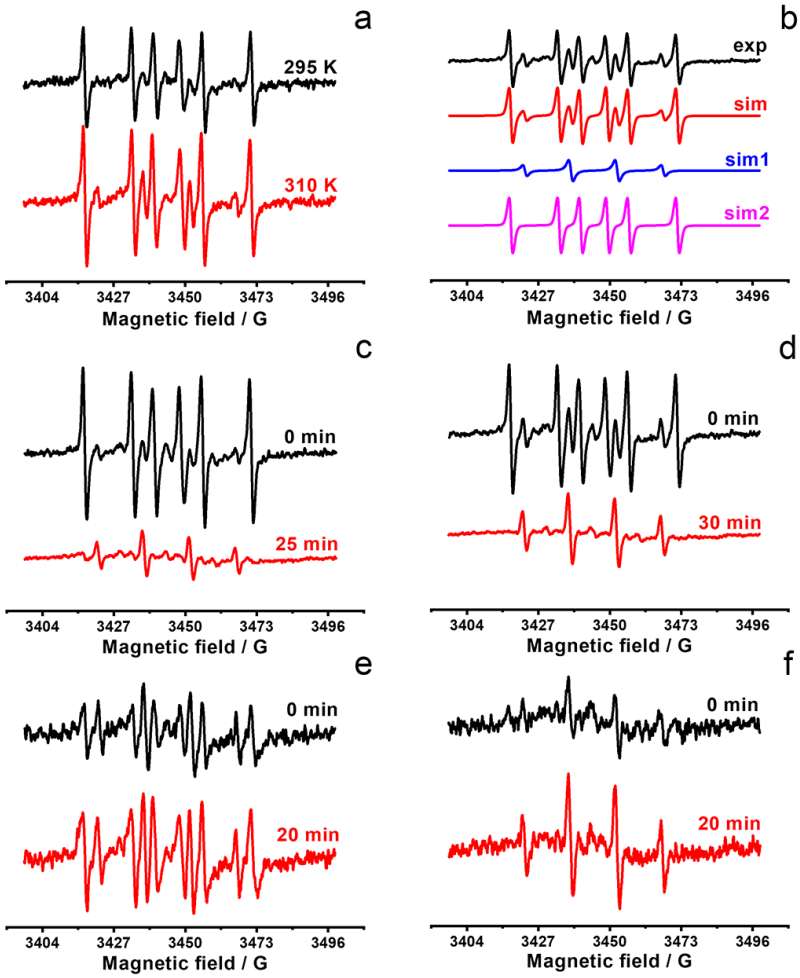


Figure 8. (**a**) ESR spectra of F-127-$Cu_2I_2L_3$ colloids at 295 K and 310 K (pH = 5.2). (**b**) Experimental (exp) and simulated (sim) spectra of F-127-$Cu_2I_2L_3$ colloids and simulated spectra of DMPO-OH· (sim1) and DMPO-R· (sim2) spin-adducts. (**c**–**f**) ESR spectra of F-127-$Cu_2I_2L_3$ colloids at pH = 5.2 (**c**), in the presence of H_2O_2 (pH = 5.2, C = 200 μM) (**d**), at pH = 7.0 (**e**) and in the presence of GSH (pH = 5.2, C = 400 μM) (**f**), recorded right after sample preparation and after 20–30 min.

As previously mentioned, the oxidative degradation of F-127-$Cu_2I_2L_3$ nanoparticles increased as the temperature increases from 293 to 310 K (Figure 6e). This correlates with the increased level of DMPO-OH· adducts generated by F-127-$Cu_2I_2L_3$ colloids when heated up to 310 K (Figure 8a). It is also worth noting the formation of DMPO-R· adducts (R· is alkyl radical) (g = 2.0055, aN = 15.6 G, aH = 22.5 G, ΔH = 0.8 G) [43] along with DMPO-OH·, which is illustrated by the simulated spectra (Figure 8b). However, DMPO-R· adducts tended to disappear within several minutes, while the level of DMPO-OH· adducts increased within this time and reaching to the saturated level (Figure 8c).

It is commonly reported that the ROS generation by Cu^I ions via the so-called Fenton reaction is triggered by H_2O_2 [44,45]; however, no significant increase in the level of DMPO-OH· adduct was observed in the solution of H_2O_2 at 200 μM (Figure 8d). Acidification is another well-known factor facilitating the Fenton-like reactions of Cu^I complexes [44], although the levels of DMPO-OH· were similar at pH = 5.2 and 7.0 (Figure 8c,e). Thus, the ROS generation by F-127-$Cu_2I_2L_3$ nanoparticles is a self-boosting process, where the colloidal and thermodynamic stability of F-127-$Cu_2I_2L_3$ prerequisites the reversibility of the Fenton reactions (1, 2). It is worth noting that the coordination of Cu^I with phosphine ligands has already been highlighted as the factor restricting $Cu^I \rightarrow Cu^{II}$ oxidation [16,17]. Thus, the specific ligand environment of Cu^I in F-127-$Cu_2I_2L_3$ nanoparticles plays a major role in the self-boosting ROS generation.

It is worth noting that the influence of GSH on the ROS generation by the aqueous colloids derives from the reductive effects on both the generated OH· and Cu^{II} represented by Equilibriums (3) and (4), respectively [36–38]. It is also worth noting that the produced oxidative form GSSG forms stable complexes with Cu^{I} ions via Equilibrium (5) [36–38].

$$2GSH + 2OH\cdot \rightleftarrows GSSG + 2H_2O \quad (3)$$

$$2Cu^{II} + 2GSH \rightleftarrows 2Cu^{I} + GSSG + 2H^{+} \quad (4)$$

$$2Cu^{I} + GSSG \rightleftarrows (Cu^{I})_2GSSG \quad (5)$$

It is worth noting that, in accordance with Equilibrium (4), the production of GSSG is pH-dependent. Thus, the effect of GSH on the level of DMPO-OH· in F-127-$Cu_2I_2L_3$ colloids (C = 40 μM) was evaluated in GSH solutions (C = 400 μM) at pH = 5.2 and 7.0 at 310 K. The addition of GSH to the as-prepared samples of F-127-$Cu_2I_2L_3$ at pH = 5.2 and 7.0 resulted in a low level of DMPO-OH· adduct without contribution of DMPO-R· (Figure 8f and Figure S11), while the ESR measurements within 15–20 min revealed differences between the samples. The level of DMPO-OH· adduct tended to increase within 20 min and reached the saturation level at pH = 5.2 (Figure 8f). The opposite situation was observed at pH = 7.0, where the signal of DMPO-OH· detected just after the addition of DMPO disappeared within 15 min (Figure S11). The low level of DMPO-OH· adduct in the as-prepared samples can be explained by the reductive effect of GSH via Equilibrium (3). However, the scavenging effect of GSH via Equilibrium (3) was overcome by further ROS generation in F-127-$Cu_2I_2L_3$ colloids at pH = 5.2. It is worth assuming the shifting to right of Equilibrium (4) under the pH increase from 5.2 to 7.0 as the reason for the additional production of GSSG, since the latter must facilitate the partial degradation of the nanoparticles through the stripping of Cu^{I} ions by the as-produced GSSG via Equilibrium (5). The increasing luminescence quenching of F-127-$Cu_2I_2L_3$ nanoparticles over time in the presence of GSH (Figure 7) agrees well with the stripping of Cu^{I} ions by the as-produced GSSG. Thus, F-127-$Cu_2I_2L_3$ nanoparticles can be regarded as promising candidates for inducing intracellular ROS generation, although the coordinative effect of the cytoplasmic GSSG can decrease the levels of ROS. It is also worth noting that the luminescence of F-127-$Cu_2I_2L_3$ nanoparticles can provide an evaluation of their cell internalization using luminescence microscopy techniques.

2.4. Cytotoxicity and Cell Internalization of F-127-$Cu_2I_2L_3$ Nanoparticles

The ability of F-127-$Cu_2I_2L_3$ to generate ROS allows us to assume that nanoparticles can induce cell apoptosis as a response to oxidative stress triggered by ROS generation. The luminescence of F-127-$Cu_2I_2L_3$ nanoparticles revealed their internalization into M-HeLa cells, which was demonstrated by the flow cytometry data (Figure 9a). The flow cytometry measurements were preceded by measuring the viability of the cell samples incubated with F-127-$Cu_2I_2L_3$ nanoparticles at different concentrations (Figure S12). The IC_{50} value of F-127-$Cu_2I_2L_3$ calculated from the cell viability data was above 100 μM, which is much greater than the IC_{50} values reported for the molecular Cu^{I} complexes [16,46,47], but it is close to the IC_{50} values reported for CuI phosphine conjugated with the peptides [17]. This highlights the formation of nanoparticulate forms of Cu^{I} complexes as a route to reduce their cytotoxicity.

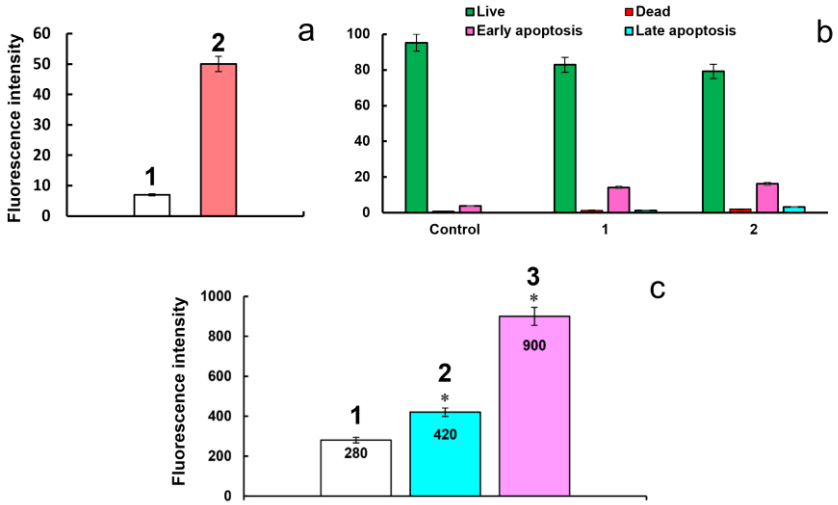


Figure 9. (**a**) Study of cellular uptake of F-127-$Cu_2I_2L_3$ by M-HeLa cells: 1—control, 2—15 μM. (**b**) Induction of apoptosis in M-HeLa cells incubated with F-127-$Cu_2I_2L_3$ at concentrations of 40 μM (1) and 80 μM (2). (**c**) The intracellular ROS generation by F-127-$Cu_2I_2L_3$: 1—control, 2—40 μM, 3—80 μM. The values are presented as mean ± SD of three independent experiments.

The analysis of the flow cytometry data indicates the predominance of apoptotic cells in the early stage (Figure 9b). In this stage, the cells shrink within a few minutes, losing up to 1/3 of their volume. The enhanced level of the intracellular ROS measured in the cells incubated with F-127-$Cu_2I_2L_3$ nanoparticles (Figure 9c) confirmed the ROS generation as the trigger of the early apoptosis. However, the observed extent of the early apoptotic cells was insignificant. One can hypothesize that the ROS levels generated by F-127-$Cu_2I_2L_3$ in the intracellular space was not enough to advance apoptosis to later stages followed by cell death.

3. Materials and Methods

3.1. Reagents and Materials

The commercial chemicals hydrogen peroxide (H_2O_2, 30%), lysine, arginine, histidine, bovine serum albumin, cysteine, glutathione (GSH), 5,5-Dimethyl-1-Pyrroline-N-Oxide (DMPO) and Pluronic F-127 were purchased from Sigma-Aldrich. N,N-Dimethylformamide (DMF) was purchased from Scharlau and distilled water was used as a solvent. Tris-(hydroxymethyl)-aminomethane (TRIS) extra pure from Scharlau, acetic-acetate, phosphate and sodium tetraborate ($Na_2B_4O_7$*10 H_2O) were used as the buffers.

The $Cu_4I_4L_2$ complex was synthesized in accordance with previously published procedures [2].

The aqueous F-127-$Cu_2I_2L_3$ colloids were obtained by the drop-wise addition of 0.6 mL of the $Cu_4I_4L_2$ complex solution in DMF (C = 1 mM) into 2.4 mL of aqueous NaI solution (C = 0.5 M) under vigorous stirring. The turbid solutions were then subjected to ultrasonic treatment for 20 min at room temperature with subsequent separation of colloids through centrifugation (15,000 rpm for 35 min at 20 °C). Then, 3 mL of F-127 aqueous solution (C = 1 g/L) was added to the precipitate and subjected to ultrasonic treatment followed by centrifugation. The ultrasonication–centrifugation procedure was repeated twice in order to remove the excess F-127. Concentrations of the resulting aqueous colloids are given in terms of copper ion content determined by the ICP-OES.

3.2. Methods

3.2.1. Dynamic Light Scattering

Dynamic light scattering (DLS) and electrokinetic potential experiments were performed using a Zetasizer Nano instrument (Malvern Instruments, Malvern, Worcestershire, UK). Electrokinetic potential values were calculated using the Smoluchowski–Helmholtz

equation [48]. Experimental autocorrelation functions were analyzed with the Malvern DTS software and the second-order cumulant expansion methods. The average error was ca. 4%. All samples were prepared in deionized water filtered through a PVDF membrane with a Syringe Filter (0.45 μm). All measurements were performed at least in triplicate at 25 °C.

3.2.2. Fluorescence Spectroscopy

The emission spectra of aqueous colloids were recorded on a fluorescence spectrophotometer Hitachi F-7100 (Tokyo, Japan) with stigmatic concave diffraction grating. Excitation of samples was performed at 330 nm or 365 nm and emission was detected at 400–640 nm. Excitation and emission spectra of dried colloids at room temperature and at 77 K were measured on a Fluorolog QM-75-22-C (Horiba) spectrofluorimeter. The temperature-dependent experiments were performed using a Janis ST-100 cryostat with a thermocontroller LakeShore 325. LED (405 nm, pulse duration 1.3 ns) was used to carry out lifetime measurements at room temperature.

3.2.3. NMR Spectroscopy

^{1}H NMR (600.1 MHz) and ^{31}P NMR (242.9 MHz) spectra were recorded using a Bruker Avance 600 spectrometer and ^{1}H NMR (400.13 MHz) and ^{31}P NMR (161.96 MHz) spectra were recorded using a Bruker Avance 400 spectrometer using the residual solvent as an internal reference for ^{1}H and 85% aqueous solution of H_3PO_4 as an external reference for ^{31}P. Chemical shifts are reported in ppm.

3.2.4. IR Spectroscopy

The infrared spectra were recorded using a Bruker Tensor 27 Fourier-transform spectrometer (Ettlingen, Germany) in the range of 4000–400 cm^{-1} with an optical resolution of 4 cm^{-1} and an accumulation of 32 scans using KBr pressed pellets.

3.2.5. ICP-OES

Cu and P ion concentrations were measured using a simultaneous inductively coupled plasma optical emission spectrometer (ICP-OES) model iCAP 6300 DUO by Varian Thermo Scientific Company equipped with a CID detector (168 Third Avenue, Waltham, MA, USA). Together, the radial and axial view configurations enabled optimal peak height measurements with suppressed spectral noise. The concentrations of Cu and P ions were determined, respectively, by the spectral lines: 324.754 and 177.495 nm. A Sc standard was used as the internal standard (10 ppm in each sample) and standards of Cu and P as calibration standards (five-point calibration).

3.2.6. ESI Measurements

ESI measurements were performed using an AmaZon X ion trap mass spectrometer (Bruker Daltonics, Bremen, Germany) in positive mode. The mass spectral data were processed using the program XCalibur. The mass spectra are given as m/z values and relative intensities (I_{rel}, %).

3.2.7. TEM Measurements

Samples were prepared as follows: a drop of 6 μL was taken from the middle of a freshly prepared solution using a dispenser (Biohit Proline Plus, Göttingen, Germany) and applied to a 300 mesh copper grid with a carbon-formvar support film (Agar Scientific, Stansted, Essex, UK). A drop completely covers the grid. The sample preparation process was carried out at room temperature. Next, the sample was dried in a muffle furnace at 80 °C. TEM images were obtained using a Hitachi HT7700 transmission electron microscope (Tokyo, Japan) at an accelerating voltage of 100 kV (direct observation state).

3.2.8. Powder X-ray Diffraction (PXRD)

PXRD measurements were performed using an automatic Bruker D8 Advance diffractometer equipped with a Vario attachment and Vantec linear PSD using Cu radiation (40 kV, 40 mA) monochromated by a curved Johansson monochromator (λ Cu Kα1 1.54063 Å) (Bruker Optik GmbH, Ettlingen, Germany). Room-temperature data were collected in the reflection mode with a flat-plate sample.

The colloidal solution was applied to a silicon plate. To increase the total amount of the sample, several more layers were applied on top of the first one after it dried. Patterns were recorded in the 2θ range between 2° and 70° in 0.008° steps with a step time of 0.1–1 s. The samples were spun (15 rpm) throughout the data collection. The processing of the obtained data was performed using EVA [49] and TOPAS [50] software packages.

3.2.9. ESR Measurements

The ESR measurements were carried out using an X-band ELEXSYS E500 ESR spectrometer. ESR spectra were simulated using a WinSim 0.96 program (developed by NIEHS). The irradiation of the samples was done by light emitting diodes (405 nm) at a distance of 5 cm from the light source. The samples were buffered (pH = 5.2 or 7.0) solutions of DMPO (C = 0.1 M) in the presence of nanoparticles (C = 40 μM) and/or H_2O_2 (C = 200 μM) and/or GSH (C = 400 μM). The measurements were performed at 295 K and 310 K.

3.2.10. Cytotoxicity Assay

Cytotoxicity of the nanoparticles on human cancer cells was assessed using the MTT test. The principle of the method is based on the reduction of tetrazolium dye (MTT)—3-(4,5-dimethylthiazol-2-yl)-2,5-diphenyl-tetrazolium bromide—by NADP-H-dependent cellular oxidoreductases to insoluble blue-violet formazan, which crystallizes inside the cell. The amount of formazan formed is proportional to the number of cells with active metabolism. Human clone M-HeLa 11, epithelioid carcinoma of the cervix, strain HeLa, clone M-HeLa from the collection of type cultures of the Institute of Cytology of the Russian Academy of Sciences was used in experiments. The cells were seeded in a 96-well plate (Nunc) at a concentration of 5×10^3 cells per well in a volume of 100 μL of medium and cultured in a CO_2 incubator at 37 °C until a monolayer was formed. Then, the nutrient medium was removed and 100 μL of solutions of the test sample in given dilutions were added to the wells, which were prepared directly in the nutrient medium with the addition of 5% DMSO to improve solubility. After 24 h of cell incubation with the test compounds, the nutrient medium was removed from the plates, 100 μL of serum-free nutrient medium with MTT at a concentration of 0.5 mg/mL was added and incubated for 4 h at 37 °C. A volume of 100 μL of DMSO was added to the formazan crystals in each well. The optical density was recorded at a wavelength of 540 nm using an Invitrologic tablet reader (Novosibirsk, Russia). The experiments were repeated three times. Untreated M-HeLa cells were used as controls.

The IC_{50} values were calculated using the online calculator MLA—Quest Graph™ IC_{50} Calculator (AAT Bioquest, Inc., Sunnyvale, CA, USA) (Version 2021) (accessed on 1 February 2023) [51]. The values calculated from the triplicate measurements were averaged.

3.2.11. Cellular Uptake Study

M-HeLa cell lines (1×10^5 cells/well) in a final volume of 500 μL were plated into 24-well plates (Eppendorf, Hamburg, Germany). After a 24 h incubation, testing compounds were added to the wells at a concentration of 15 μM and incubated for 24 h under CO_2. Cellular uptake was analyzed by flow cytometry (Guava easy Cyte 8HT, MERCK, Kenilworth, NJ, USA). Untreated cells were used as a negative control. The studies were carried out in triplicate. The values are presented as the mean ± SD ($p < 0.05$).

3.2.12. Cell Apoptosis Analysis

M-HeLa cells (1×10^6 cells / well) in a final volume of 2 mL were seeded into 6-well plates. After a 24 h incubation, testing compounds were added to wells. The cells were harvested at 2000 rpm for 5 min and then washed twice with ice-cold PBS (4 °C), followed by resuspension in 100 μL binding buffer. Next, the samples were incubated with 0.35 μL Annexin V-Alexa Fluor 647 and 0.1 μL PI for 40 min at room temperature in the dark. Finally, the cells were analyzed by flow cytometry (Guava easy Cyte, MERCK, Kenilworth, NJ, USA). Untreated cells were used as the control. A total of 20,000 events were analyzed in the apoptotic assay. The studies were carried out in triplicate. The values are presented as the mean ± SD ($p < 0.01$).

3.2.13. Detection of Intracellular ROS

M-HeLa cells were incubated with testing compounds at concentrations of 40 μM and 80 μM for 24 h. ROS generation was investigated using flow cytometry and the CellROX® Deep Red flow cytometry kit. For this, M-HeLa cells were harvested at 2000 rpm for 5 min and then washed twice with ice-cold PBS (4 °C), followed by resuspension in 0.1 mL of medium without FBS, to which 0.2 μL of CellROX® Deep Red was added and incubated at 37 °C for 30 min. After washing the cells three times and suspending them in PBS, the production of ROS in the cells was immediately monitored using a flow cytometer (Guava easy Cyte, MERCK, Kenilworth, USA). The experiments were repeated three times. Data are presented as mean ± SD ($p < 0.05$).

4. Conclusions

The obtained results highlight the 1,3-bis(benzhydryl)-5-(pyridine-2-yl)-1,3-diaza-5-phosphacyclohexane ligand as the convenient environment for Cu_nI_n halide cores, providing chemical safety in the aqueous conditions. However, the initial $Cu_4I_4L_2$ complex undergoes transformation into the $Cu_2I_2L_3$ form in the specific aqueous-organic solutions, triggering the formation of the $Cu_2I_2L_3$ complex-based nanoparticles exhibiting green luminescence in both the dried state and in aqueous solutions. The spectral analysis of the dried colloids revealed both coordinated and non-coordinated moieties of the ligand.

The unique luminescent characteristics of $Cu_2I_2L_3$-based nanoparticles arising from the ^{3}(M+X)LCT transition from the cluster core allows to monitor their resistance to oxidative degradation at various concentrations, pHs, time points and temperature conditions. The as-prepared colloids can be used even after storage for 1.5 months at the specific concentration conditions. Both the increase in temperature from 293 to 310 K and dilution of the aqueous $Cu_2I_2L_3$-based colloids are prerequisites for the oxidative degradation of the nanoparticles via the Fenton-type reactions. Similar levels of ROS generation were observed in the buffered solutions (pH = 5.2 and 7.0) at 310 K, although the ten-fold excess of glutathione at pH = 7.0 was enough to restrict the ROS generation.

The luminescence of F-127-$Cu_2I_2L_3$ nanoparticles allows the visualization of their internalization into cells, while the cell viability measurements revealed the low cytotoxicity of the colloids. The fluorescent analysis of the cell samples incubated with the colloids revealed intracellular ROS generation followed by the appearance of the cells in the early apoptotic stage with an insignificant contribution of cells in the late stage. Thus, the developed Cu^I complex-based nanoparticles can be applied in both cell labeling and triggering apoptotic processes, although their stability is too high for significant cytotoxicity.

Supplementary Materials: The following supporting information can be downloaded at: https://www.mdpi.com/article/10.3390/inorganics11040141/s1. Figure S1. ^{1}H NMR spectrum of the $Cu_4I_4L_2$ complex in DMF-d_7. Figure S2. ^{1}H NMR spectrum of the $Cu_4I_4L_2$ complex in acetone-d_6. Figure S3. ^{1}H NMR spectrum of the precipitated Cu^I complex, dissolved in DMF-d_7. Inset: ^{31}P NMR spectrum of the same sample in DMF-d_7. Figure S4. Simulated and experimental (insets) ESI-mass spectra of $Cu_4I_4L_2$ complex, dissolved in DMF-d_7. Figure S5. Simulated and experimental (inset) ESI-mass spectra of precipitated Cu^I complex, dissolved in DMF-d_7. Table S1. ICP-OES data for F-127-

$Cu_2I_2L_3$ colloids and supernatant. Figure S6. Calculated PXRD patterns for different crystalline solvates of $Cu_4I_4L_2$ complex: acetone (1), acetonitrile (2), benzene (3) and dichloromethane (4). The curves are shifted along the intensity axis for clarity. Figure S7. Luminescence of F-127-$Cu_2I_2L_3$ colloids (C = 200 μM) obtained from different $Cu_4I_4L_2$ complex powders: directly synthesized (1) and recrystallized from acetonitrile (2) and acetone (3). λ_{ex} = 365 nm. Table S2. Average diameter values (d_{av}) and those evaluated through the size distribution by number (d_{num}) measured by DLS, polydispersity indices (PDI) and electrokinetic potentials (ζ) of F-127-$Cu_2I_2L_3$ nanoparticles obtained from different $Cu_4I_4L_2$ complex powders. Figure S8. Time-resolved luminescence spectrum of F-127-$Cu_2I_2L_3$ colloids (C = 200 μM). Figure S9. Luminescence intensity of F-127-$Cu_2I_2L_3$ colloids (C = 200 μM) at different temperatures: 1-2-3 – first heating-cooling cycle, 3-4-5 – second heating-cooling cycle. λ_{ex}=365 nm. Figure S10. Luminescence spectra of F-127-$Cu_2I_2L_3$ colloids (C = 40 μM) in the presence of different concentrations of lysine (a), arginine (b), histidine (c), bovine serum albumin (d) and cysteine (e). pH = 7.0, λ_{ex} = 330 nm. Figure S11. ESR spectra of F-127-$Cu_2I_2L_3$ colloids (C = 40 μM) in the presence of ten-fold excess of GSH at pH = 7.0, recorded right after the sample preparation and after 15 minutes. Figure S12. Viability of M-HeLa cells incubated with different concentrations of F-127-$Cu_2I_2L_3$ nanoparticles. The error bars represent standard deviation of the mean values.

Author Contributions: Conceptualization, A.R.M.; Formal analysis, B.A.F., J.G.E., A.T.G., K.V.K., I.R.N., S.K.A., A.D.V., V.M.B. and T.P.G.; Investigation, B.A.F., J.G.E., I.D.S., K.V.K., I.R.N., S.K.A., A.D.V. and T.P.G.; Methodology, B.A.F.; Project administration, O.G.S.; Resources, K.D.A., I.D.S. and A.A.K.; Supervision, A.R.M.; Validation, A.A.K. and O.G.S.; Visualization, B.A.F.; Writing—original draft, B.A.F. and A.R.M.; Writing—review and editing, B.A.F. and A.R.M. All authors have read and agreed to the published version of the manuscript.

Funding: This research was funded by the Russian Science Foundation, grant number 19-13-00163-P.

Data Availability Statement: Not applicable.

Acknowledgments: The authors are grateful to the Assigned Spectral-Analytical Center of the FRC Kazan Scientific Center of RAS for technical assistance.

Conflicts of Interest: The authors declare no conflict of interest.

References

1. Yin, S.Y.; Wang, Z.; Liu, Z.M.; Yu, H.J.; Zhang, J.H.; Wang, Y.; Mao, R.; Pan, M.; Su, C.Y. Multiresponsive UV-one-photon absorption, near-infrared-two-photon absorption, and X/γ-photoelectric absorption luminescence in one [Cu_4I_4] compound. *Inorg. Chem.* **2019**, *58*, 10736–10742. [CrossRef] [PubMed]
2. Strelnik, I.; Shamsieva, A.; Akhmadgaleev, K.; Gerasimova, T.; Dayanova, I.; Kolesnikov, I.; Fayzullin, R.; Islamov, D.; Musina, E.; Karasik, A.; et al. Emission and Luminescent Vapochromism Control of Octahedral Cu_4I_4 Complexes by Conformationally Restricted P,N Ligands. *Chem. Eur. J.* **2022**, *29*, e202202864. [CrossRef]
3. Artem'ev, A.V.; Baranov, A.Y.; Rakhmanova, M.I.; Malysheva, S.F.; Samsonenko, D.G. Copper(I) halide polymers derived from tris[2-(pyridin-2-yl)ethyl]phosphine: Halogen-tunable colorful luminescence spanning from deep blue to green. *New J. Chem.* **2020**, *44*, 6916–6922. [CrossRef]
4. Boden, P.; Di Martino-Fumo, P.; Busch, J.M.; Rehak, F.R.; Steiger, S.; Fuhr, O.; Nieger, M.; Volz, D.; Klopper, W.; Brase, S.; et al. Investigation of Luminescent Triplet States in Tetranuclear CuI Complexes: Thermochromism and Structural Characterization. *Chem. Eur. J.* **2021**, *27*, 5439–5452. [CrossRef] [PubMed]
5. Liu, Z.; Djurovich, P.I.; Whited, M.T.; Thompson, M.E. Cu_4I_4 clusters supported by P∧N-type ligands: New structures with tunable emission colors. *Inorg. Chem.* **2012**, *51*, 230–236. [CrossRef]
6. Liu, G.N.; Zhao, R.Y.; Xu, R.D.; Zhang, X.; Tang, X.N.; Dan, Q.J.; Wei, Y.W.; Tu, Y.Y.; Bo, Q.B.; Li, C. A novel tetranuclear copper (I) iodide metal–organic cluster [Cu_4I_4(Ligand)$_5$] with highly selective luminescence detection of antibiotic. *Cryst. Growth Des.* **2018**, *18*, 5441–5448. [CrossRef]
7. Xin, X.L.; Chen, M.; Ai, Y.B.; Yang, F.L.; Li, X.L.; Li, F. Aggregation-induced emissive copper (I) complexes for living cell imaging. *Inorg. Chem.* **2014**, *53*, 2922–2931. [CrossRef]
8. Shamsieva, A.V.; Kolesnikov, I.E.; Strelnik, I.D.; Gerasimova, T.P.; Kalinichev, A.A.; Katsyuba, S.A.; Musina, E.I.; Lahderanta, E.; Karasik, A.A.; Sinyashin, O.G. Fresh look on the nature of dual-band emission of octahedral copper-iodide clusters—Promising ratiometric luminescent thermometers. *J. Phys. Chem. C* **2019**, *123*, 25863–25870. [CrossRef]
9. Kang, Z.; Wu, C.; Dong, L.; Liu, W.; Mou, J.; Zhang, J.; Chang, Z.; Jiang, B.; Wang, G.; Kang, F.; et al. 3D porous copper skeleton supported zinc anode toward high capacity and long cycle life zinc ion batteries. *ACS Sustain. Chem. Eng.* **2019**, *7*, 3364–3371. [CrossRef]

10. Santini, C.; Pellei, M.; Gandin, V.; Porchia, M.; Tisato, F.; Marzano, C. Advances in copper complexes as anticancer agents. *Chem. Rev.* **2014**, *114*, 815–862. [CrossRef]
11. Komarnicka, U.K.; Kozieł, S.; Zabierowski, P.; Kruszyński, R.; Lesiow, M.K.; Tisato, F.; Porchia, M.; Kyzioł, A. Copper (I) complexes with phosphines P(p-OCH_3-Ph)$_2CH_2OH$ and P(p-OCH_3-Ph)$_2CH_2$SarGly. Synthesis, multimodal DNA interactions, and prooxidative and in vitro antiproliferative activity. *J. Inorg. Biochem.* **2020**, *203*, 110926. [CrossRef]
12. Gandin, V.; Ceresa, C.; Esposito, G.; Indraccolo, S.; Porchia, M.; Tisato, F.; Santini, C.; Pellei, M.; Marzano, C. Therapeutic potential of the phosphino Cu (I) complex (HydroCuP) in the treatment of solid tumors. *Sci. Rep.* **2017**, *7*, 13936. [CrossRef]
13. Luo, C.L.; Hu, C.X.; Shang, P.; Wen, G.Z.; Zhu, J.J.; Xuan, Y.H.; Xia, B.L.; Liu, Y.C.; Jiang, Z.H.; Dong, G.; et al. Synthesis of heteroleptic phosphine–copper (I) complexes: Fluorescence sensing and catalytic properties. *New J. Chem.* **2021**, *45*, 8910–8917. [CrossRef]
14. Fanizza, E.; Mastrogiacomo, R.; Pugliese, O.; Guglielmelli, A.; De Sio, L.; Castaldo, R.; Scavo, M.P.; Giancaspro, M.; Rizzi, F.; Gentile, G.; et al. NIR-Absorbing Mesoporous Silica-Coated Copper Sulphide Nanostructures for Light-to-Thermal Energy Conversion. *Nanomaterials* **2022**, *12*, 2545. [CrossRef] [PubMed]
15. Fedorenko, S.; Farvaeva, D.; Stepanov, A.; Bochkova, O.; Kholin, K.; Nizameev, I.; Drobyshev, S.; Gerasimova, T.; Voloshina, A.; Fanizza, E.; et al. Tricks for organic-capped $Cu_{2-x}S$ nanoparticles encapsulation into silica nanocomposites co-doped with red emitting luminophore for NIR activated-photothermal/chemodynamic therapy. *J. Photochem. Photobiol. A* **2022**, *433*, 114187. [CrossRef]
16. Komarnicka, U.K.; Pucelik, B.; Wojtala, D.; Lesiów, M.K.; Stochel, G.; Kyzioł, A. Evaluation of anticancer activity in vitro of a stable copper (I) complex with phosphine-peptide conjugate. *Sci. Rep.* **2021**, *11*, 23943. [CrossRef]
17. Komarnicka, U.K.; Kozieł, S.; Starosta, R.; Kyzioł, A. Selective Cu (I) complex with phosphine-peptide (SarGly) conjugate contra breast cancer: Synthesis, spectroscopic characterization and insight into cytotoxic action. *J. Inorg. Biochem.* **2018**, *186*, 162–175. [CrossRef]
18. Kyzioł, A.; Cierniak, A.; Gubernator, J.; Markowski, A.; Jeżowska-Bojczuk, M.; Komarnicka, U.K. Copper (I) complexes with phosphine derived from sparfloxacin. Part III: Multifaceted cell death and preliminary study of liposomal formulation of selected copper (I) complexes. *Dalton Trans.* **2018**, *47*, 1981–1992. [CrossRef] [PubMed]
19. Elistratova, J.; Faizullin, B.; Strelnik, I.; Gerasimova, T.; Khairullin, R.; Sapunova, A.; Voloshina, A.; Mukhametzyanov, T.; Musina, E.; Karasik, A.; et al. Impact of oppositely charged shell and cores on interaction of core-shell colloids with differently charged proteins as a route for tuning of the colloids cytotoxicity. *Colloids Surf. B* **2020**, *196*, 111306. [CrossRef]
20. Zhang, K.; Meng, X.; Yang, Z.; Dong, H.; Zhang, X. Enhanced cancer therapy by hypoxia-responsive copper metal-organic frameworks nanosystem. *Biomaterials* **2020**, *258*, 120278. [CrossRef]
21. Zhao, R.M.; Guo, Y.; Yang, H.Z.; Zhang, J.; Yu, X.Q. Zn-Promoted gene transfection efficiency for non-viral vectors: A mechanism study. *New J. Chem.* **2021**, *45*, 13549–13557. [CrossRef]
22. Lin, G.; Zhang, Y.; Zhang, L.; Wang, J.; Tian, Y.; Cai, W.; Tang, S.; Chu, C.; Zhou, J.J.; Mi, P.; et al. Metal-organic frameworks nanoswitch: Toward photo-controllable endo/lysosomal rupture and release for enhanced cancer RNA interference. *Nano Res.* **2020**, *13*, 238–245. [CrossRef]
23. Tian, H.; Zhang, M.; Jin, G.; Jiang, Y.; Luan, Y. Cu-MOF chemodynamic nanoplatform via modulating glutathione and H_2O_2 in tumor microenvironment for amplified cancer therapy. *J. Colloid Interface Sci.* **2021**, *587*, 358–366. [CrossRef]
24. Hwang, E.; Jung, H.S. Metal–organic complex-based chemodynamic therapy agents for cancer therapy. *Chem. Commun.* **2020**, *56*, 8332–8341. [CrossRef]
25. Ma, B.; Wang, S.; Liu, F.; Zhang, S.; Duan, J.; Li, Z.; Kong, Y.; Sang, Y.; Liu, H.; Bu, W.; et al. Self-assembled copper–amino acid nanoparticles for in situ glutathione "AND" H_2O_2 sequentially triggered chemodynamic therapy. *J. Am. Chem. Soc.* **2018**, *141*, 849–857. [CrossRef] [PubMed]
26. Enikeeva, K.R.; Shamsieva, A.V.; Strelnik, A.G.; Fayzullin, R.R.; Zakharychev, D.V.; Kolesnikov, I.E.; Dayanova, I.R.; Gerasimova, T.P.; Strelnik, I.D.; Musina, E.I.; et al. Green Emissive Copper (I) Coordination Polymer Supported by the Diethylpyridylphosphine Ligand as a Luminescent Sensor for Overheating Processes. *Molecules* **2023**, *28*, 706. [CrossRef]
27. Elistratova, J.; Faizullin, B.; Shamsutdinova, N.; Gubaidullin, A.; Strelnik, I.; Babaev, V.; Kholin, K.; Nizameev, I.; Musina, E.; Khairullin, R.; et al. Synthesis of Au (I) complex-based aqueous colloids for sensing of biothiols. *Inorg. Chim. Acta* **2019**, *485*, 26–32. [CrossRef]
28. Podyachev, S.N.; Zairov, R.R.; Mustafina, A.R. 1,3-Diketone calix[4]arene derivatives—A new type of versatile ligands for metal complexes and nanoparticles. *Molecules* **2021**, *26*, 1214. [CrossRef] [PubMed]
29. Musina, E.I.; Shamsieva, A.V.; Strelnik, I.D.; Gerasimova, T.P.; Krivolapov, D.B.; Kolesnikov, I.E.; Grachova, E.V.; Tunik, S.P.; Bannwarth, C.; Grimme, S.; et al. Synthesis of novel pyridyl containing phospholanes and their polynuclear luminescent copper (I) complexes. *Dalton Trans.* **2016**, *45*, 2250–2260. [CrossRef] [PubMed]
30. Zink, D.M.; Baumann, T.; Friedrichs, J.; Nieger, M.; Bräse, S. Copper (I) complexes based on five-membered P∧N heterocycles: Structural diversity linked to exciting luminescence properties. *Inorg. Chem.* **2013**, *52*, 13509–13520. [CrossRef]
31. Zink, D.M.; Volz, D.; Baumann, T.; Mydlak, M.; Flügge, H.; Friedrichs, J.; Nieger, M.; Bräse, S. Heteroleptic, dinuclear copper (I) complexes for application in organic light-emitting diodes. *Chem. Mater.* **2013**, *25*, 4471–4486. [CrossRef]
32. Mondal, R.; Lozada, I.B.; Davis, R.L.; Williams, J.G.; Herbert, D.E. Exploiting synergy between ligand design and counterion interactions to boost room temperature phosphorescence from Cu (I) compounds. *J. Mater. Chem. C* **2019**, *7*, 3772–3778. [CrossRef]

33. Hofbeck, T.; Niehaus, T.A.; Fleck, M.; Monkowius, U.; Yersin, H. P∩N Bridged Cu (I) Dimers Featuring Both TADF and Phosphorescence. From Overview towards Detailed Case Study of the Excited Singlet and Triplet States. *Molecules* **2021**, *26*, 3415. [CrossRef] [PubMed]
34. Zink, D.M.; Bächle, M.; Baumann, T.; Nieger, M.; Kühn, M.; Wang, C.; Klopper, W.; Monkowius, U.; Hofbeck, T.; Yersin, H.; et al. Synthesis, structure, and characterization of dinuclear copper (I) halide complexes with P^N ligands featuring exciting photoluminescence properties. *Inorg. Chem.* **2013**, *52*, 2292–2305. [CrossRef]
35. Abbas, K.; Babić, N.; Peyrot, F. Use of spin traps to detect superoxide production in living cells by electron paramagnetic resonance (EPR) spectroscopy. *Methods* **2016**, *109*, 31–43. [CrossRef] [PubMed]
36. Aliaga, M.E.; López-Alarcón, C.; Bridi, R.; Speisky, H. Redox-implications associated with the formation of complexes between copper ions and reduced or oxidized glutathione. *J. Inorg. Biochem.* **2016**, *154*, 78–88. [CrossRef]
37. Walsh, M.J.; Ahner, B.A. Determination of stability constants of Cu (I), Cd (II) & Zn (II) complexes with thiols using fluorescent probes. *J. Inorg. Biochem.* **2013**, *128*, 112–123. [CrossRef] [PubMed]
38. Morgan, M.T.; Nguyen, L.A.H.; Hancock, H.L.; Fahrni, C.J. Glutathione limits aquacopper (I) to sub-femtomolar concentrations through cooperative assembly of a tetranuclear cluster. *J. Biol. Chem.* **2017**, *292*, 21558–21567. [CrossRef] [PubMed]
39. Xiong, Y.; Xiao, C.; Li, Z.; Yang, X. Engineering nanomedicine for glutathione depletion-augmented cancer therapy. *Chem. Soc. Rev.* **2021**, *50*, 6013–6041. [CrossRef]
40. Carini, M.; Aldini, G.; Orioli, M.; Facino, R.M. Electron paramagnetic resonance (EPR) spectroscopy: A versatile and powerful tool in pharmaceutical and biomedical analysis. *Curr. Pharm. Anal.* **2006**, *2*, 141–159. [CrossRef]
41. Angelé-Martínez, C.; Nguyen, K.V.T.; Ameer, F.S.; Anker, J.N.; Brumaghim, J.L. Reactive oxygen species generation by copper (II) oxide nanoparticles determined by DNA damage assays and EPR spectroscopy. *Nanotoxicology* **2017**, *11*, 278–288. [CrossRef]
42. Hedrick, W.R.; Webb, M.D.; Zimbrick, J.D. Spin trapping of reactive uracilyl radicals produced by ionizing radiation in aqueous solutions. *Int. J. Radiat. Biol. Relat. Stud. Phys. Chem. Med.* **1982**, *41*, 435–442. [CrossRef] [PubMed]
43. Kirino, Y.; Ohkuma, T.; Kwan, T. Spin trapping with 5,5-dimethylpyrroline-N-oxide in aqueous solution. *Chem. Pharm. Bull.* **1981**, *29*, 29–34. [CrossRef]
44. Luo, B.; Chen, L.; Hong, Z.; You, X.; Huang, F.P.; Bian, H.D.; Zhang, L.; Zhao, S. A simple and feasible atom-precise biotinylated Cu (I) complex for tumor-targeted chemodynamic therapy. *Chem. Commun.* **2021**, *57*, 6046–6049. [CrossRef] [PubMed]
45. Naqvi, K.R.; Marsh, J.; Chechik, V. Formation of self-inhibiting copper (II) nanoparticles in an autocatalytic Fenton-like reaction. *Dalton Trans.* **2014**, *43*, 4745–4751. [CrossRef]
46. Bykowska, A.; Komarnicka, U.K.; Jeżowska-Bojczuk, M.; Kyzioł, A. Cu^{I} and Cu^{II} complexes with phosphine derivatives of fluoroquinolone antibiotics—A comparative study on the cytotoxic mode of action. *J. Inorg. Biochem.* **2018**, *181*, 1–10. [CrossRef]
47. Hu, J.; Mao, R.; Wang, R.; Ruan, H.; Zhao, X.; Li, K.; Guo, Y. Cu(I)-benzimidazole complexes with triphenylphosphine as coligand: DNA lesion and reactive oxygen-dependent mitochondrial dysfunction inducing apoptosis. *Inorg. Chim. Acta* **2023**, *546*, 121333. [CrossRef]
48. Delgado, A.V.; Gonzalez-Caballero, F.; Hunter, R.J.; Koopal, L.K.; Lyklema, J. Measurement and interpretation of electro-kinetic phenomena. *J. Colloid Interface Sci.* **2007**, *309*, 194–224. [CrossRef]
49. Bruker AXS. *DIFFRAC Plus Evaluation Package EVA, Version 11, User's Manual*; Bruker AXS: Karlsruhe, Germany, 2005; 258p.
50. Bruker AXS. *TOPAS V3: General Profile and Structure Analysis Software for Powder Diffraction Data*; Technical Reference; Bruker AXS: Karlsruhe, Germany, 2005; 117p.
51. AAT Bioquest, Inc. Quest Graph™ IC50 Calculator. Available online: https://www.aatbio.com/tools/ic50-calculator (accessed on 1 February 2023).

Disclaimer/Publisher's Note: The statements, opinions and data contained in all publications are solely those of the individual author(s) and contributor(s) and not of MDPI and/or the editor(s). MDPI and/or the editor(s) disclaim responsibility for any injury to people or property resulting from any ideas, methods, instructions or products referred to in the content.